Strain and vorticity analysis using small-scale faults and associated drag folds

Enrique Gomez-Rivas[a,*], Paul D. Bons[b], Albert Griera[c], Jordi Carreras[a], Elena Druguet[a] and Lynn Evans[d]

[a]*Departament de Geologia, Universitat Autònoma de Barcelona, 08193 Bellaterra (Barcelona), Spain*

[b]*Mineralogie und Geodynamik, Institut für Geowissenschaften, Eberhard Karls Universität, Sigwartstr. 10, 72076 Tübingen, Germany*

[c]*Laboratoire des Mécanismes et Transferts en Géologie, Université Paul-Sabatier, 14 Ave Edouard Belin, 31400 Toulouse cedex, France*

[d]*School of Earth Sciences, University of Melbourne, Victoria, 3010, Australia*

[*] *Corresponding author. Tel: +34-935811163; Fax: +34-935811263; E-mail address: enrique@gomez-rivas.info*

Abstract

Small-scale faults with associated drag folds in brittle-ductile rocks can retain detailed information on the kinematics and amount of deformation the host rock experienced. Measured fault orientation (α), drag angle (β) and the ratio of the thickness of deflected layers at the fault (L) and further away (T) can be compared with α, β and L/T values that are calculated with a simple analytical model. Using graphs or a numerical best-fit routine, one can then determine the vorticity and initial fault orientation that best fits the data. The proposed method was successfully tested on both analogue experiments and numerical simulations with BASIL. Using this method, a kinematic vorticity number of one (dextral simple shear) and a minimum finite strain of 2.47 to 3.76 was obtained for a population of antithetic faults with associated drag folds in a case study area at Mas Rabassers de Dalt on Cap de Creus in the Variscan of the easternmost Pyrenees, Spain.

Keywords: strain analysis; vorticity; progressive deformation; faults; drag folds; foliation.

1. Introduction

One of the aims of structural geology is to determine and quantify the amount and type of deformation that rocks experienced. For this structural geologist use a variety of structures that record deformation, such as folds, boudins, veins, etc. (e.g. Ramsay and Huber, 1983). In this paper we propose a new method to determine finite strain and the kinematics of deformation using isolated, discrete small-scale faults and their associated drag folds.

Slip along a fault will cause heterogeneous deformation in the vicinity of the fault. Drag folds are the usual result in foliated rocks. Recently, much attention has been given to small-scale faults and their associated drag folds in mostly ductile rocks (Passchier, 2001; Grasemann and Stuwe, 2001; Grasemann et al., 2003; Exner et al., 2004; Grasemann et al., 2005; Wiesmayr and Grasemann, 2005; Coelho at al., 2005; Kocher and Mancktelow, 2006). In the modern literature, these structures were first described by Gayer et al. (1978) and Hudleston (1989). These structures were later dubbed "flanking folds" or "flanking structures" by Passchier (2001), who used this term for a variety of structures apart from fault-related drag folds. Instead of this new terminology, we prefer to use well-known and long-used terms: faults and drag folds.

The aforementioned authors described a range of drag fold structures and proposed a number of classification schemes. Basically, an isolated fault with its associated drag folds falls into one of four categories by the combination of two parameters: fault movement is antithetic (a-type of Grasemann et al., 2003) or synthetic (s-type) with regard to the far-field sense of shear, and drag folds are normal or reverse with regard to the slip along the fault. Of these four, the antithetic reverse-drag category is the most common for isolated faults. The fact that reverse drag is common is to be expected for isolated faults in an otherwise homogeneously deforming medium. A straight foliation element (layering, cleavage) that is cut by the fault will remain on a single straight plane away from the fault, whereas close to the fault, it is bent by the fault movement (Fig. 1a). Both synthetic and antithetic faults will therefore initially develop reverse-drag folds. However, Exner et al. (2004) showed that the slip direction may change at a high strain and reverse drag folds then become normal drag folds.

An isolated, discrete fault will typically develop drag folds with a constant sign of curvature. In a ductile shear band (i.e. minor shear zone) the foliation is not cut by a fault, but can be traced continuously through the shear band (Fig. 1b). This implies that there is an inflexion point where curvature changes sign (Coelho et al., 2005). This produces shear-band type structures in the terminology of Wiesmayr and Grasemann (2005). However, these structures still exhibit the same reverse or normal drag on a larger scale than the deflection caused by the localised shearing within the shear band. These reverse-drag folds can usually not be discerned when shear band spacing is on the same scale as the reverse drag folds.

Despite the several field studies (Gayer et al., 1978; Druguet et al., 1997; Harris, 2003), as well as numerical (Grasemann and Stüwe, 2001; Grasemann et al., 2003; Grasemann et al., 2005; Wiesmeyer and Grasemann, 2005; Coelho et al., 2005; Kocher and Mancktelow, 2006) and experimental simulations (Hudleston, 1989; Odonne, 1990; Koyi and Skelton, 2001; Harris et al., 2002; Exner et al., 2004; Kocher and Mancktelow, 2006) of drag fold structures, so far only Kocher and Mancktelow (2005) proposed a way to use these structures to quantify the finite strain and kinematics of deformation. They employed the analytical solution of Schmid and Podladchikov (2003) for the deformation field along an isolated fault that itself is passively deformed by the applied bulk flow. Their method is essentially applying the reverse model strain field to straighten out the foliation. Since bulk deformation kinematics and finite strain are not known *a priori*, a range of finite strains and vorticities are applied and the one that best straightens the foliation is chosen as the solution. The advantage of the method is that a single structure can be used to determine the vorticity of deformation, the finite strain since formation of the fault, and the original orientation of the fault relative to the foliation. A disadvantage is that appropriate software is needed.

In this paper we propose a similar method to determine these three parameters. The advantage of our proposed method is that the method does not necessarily require a computer. Instead, charts can be used, which means the method can easily be applied in the field. However, a more accurate determination can only be achieved with a computer program that is also described in this paper. A disadvantage is that multiple fault-drag fold structures are needed at different stages of development (finite strain since formation). This study is based on a population of drag fold structures in deformed quartzites from Mas Rabassers de Dalt on the Cap de Creus Peninsula in north-eastern Spain (Fig. 2). These structures and their setting will be described first to provide the background for the method that is described in the subsequent sections.

2. Examples from the Rabassers quartzite

2.1. Regional setting of the Mas Rabassers de Dalt locality

The Cap de Creus Peninsula is the easternmost outcrop of the Variscan basement exposed along the Axial Zone of the Pyrenees (Barnolas and Chiron, 1996; Carreras, 2001). The dominant lithology in the area of interest near the ruin of Mas Rabassers de Dalt (UTM 31N 0523100, 4685200, Fig. 3) is a monotonous series of amphibolite-facies meta-turbidites (Druguet, 1997; 2001). The rocks experienced multiple deformation phases during the Variscan Orogeny (Druguet, 1997; Druguet, 2001; Bons et al., 2004). Some quartzite beds, ranging from a few tens of centimetres to a few metres in thickness, are intercalated in the meta-turbidites. They form the only marker horizons that can be traced over distances of up to a few hundred metres. All the drag fold structures discussed in this paper were found in one such bed, which has a distinct black-and-white cm-scale banding (Fig. 2). The banding is layer-parallel and therefore assumed to be original sedimentary layering. The colour difference is a result of different amounts of graphite and other impurities, which also results in a difference in grain size between the layers (Fig. 2e-f). There are no indications for any significant differences in rheological properties between the dark and light bands (no cuspate-lobate structures, buckle folds in specific layers, etc.).

Near Mas Rabassers de Dalt, the quartzite and S_1 layer-parallel foliation are affected by two folding events (D_2 and D_3), resulting in a complex exposure pattern (Druguet, 1997). Pegmatites that intruded during peak-metamorphic conditions (Druguet and Hutton, 1998) are only affected by D_3 folding and shearing. The refolded folds are transected by steep, roughly NNW-SSE trending retrograde dextral shear zones (Carreras, 2001; Fusseis et al., 2006). These shear zones are associated with localization of late D_3 folding (Carreras and Casas, 1987; Carreras et al., 2005).

2.2. Drag fold structures

The discrete faults with drag folds are mainly found in the refolded quartzite bed. Within that bed they only occur in sections of the bed that run roughly parallel to the D_3 shear zones. This suggests that they formed during D_3 dextral shearing and not during earlier deformation events.

The drag folds form at cm-scale, steeply plunging faults, best seen on gently dipping outcrop surfaces. Almost all drag folds are reverse. Faults with the least offset relative to their length are almost perpendicular to the banding in the quartzite (Fig 2a). More evolved structures make an increasingly smaller angle with the banding, suggesting the structures progressively rotated clockwise (Fig. 2b). Fault tips can rarely be discerned, as faults tend to bend in a listric form to become parallel to the banding at both ends. Dextral layer-parallel slip is observed in a few rare cases where crosscutting veins are offset. Clockwise rotation of the faults and layer-parallel slip all indicate dextral shear. The faults are therefore interpreted as antithetic faults. Synthetic faults (Fig. 2c) are rare in the quartzite, and usually make a small angle with the banding. In the third dimension, the small faults are remarkably straight and may extend over more than a metre (Fig. 2d). Even on the microscopic scale, the faults are discrete planes with only a very narrow damage zone (Fig. 2e-f).

3. Method

The method described below is aimed at estimating the vorticity and finite strain that the rock experienced using parameters of the drag fold structures that can be measured easily. The following parameters can be determined in the field (Fig. 4): the angle (α) between the fault and the far-field foliation, the drag angle (β) between the foliation and the fault measured at the fault, preferably in the middle of the fault, and finally the ratio between the thickness of a marker layer at the fault, measured parallel to the fault (L) at the fault, and perpendicular to the layer (T) away from the fault. All parameters must be measured in the plane perpendicular to the fault and foliation.

The first main assumption is that the fault acts as a passive, straight marker line that is being rotated and stretched/shortened by the applied bulk flow. This assumption is validated by both numerical and physical experiments (Grasemann and Stüwe, 2001; Exner et al., 2004). Clearly, the four parameters will evolve from their initial values ($\alpha_0=\beta_0$ and $L_0/T_0=1/\sin(\alpha_0)$), depending on the flow field relative to the initial orientation of the fault and foliation. We need to know how α, β and L/T evolve, as a function of progressive deformation and initial conditions, to determine which initial conditions, kinematics of flow and finite strain lead to the combinations of α, β and L/T that were measured in the field. However, there may not be a unique solution for any given single combination of α, β and L/T. This brings us to the second main assumption for the proposed method: during progressive deformation faults form at different stages, but with the same initial orientation (α_0). At the end of deformation (the state observed in the field), each fault experienced different amounts of deformation and is therefore in a different state of development (Fig. 2a-c). Analysis of several of such faults produces a number of different α, β and L/T combinations. These measured combinations should lie on a path in α, β and L/T space that is unique to the flow kinematics and initial orientation of the faults.

The basic idea of our proposed method is that theoretical paths for all flow kinematics and initial fault orientations can be determined, and can then be compared with α, β and L/T data sets that are measured in the field. The path that best fits the data provides us with the flow kinematics and the initial fault orientation. It also allows us to determine which data point represents the highest strain, which gives a minimum estimate of the finite strain. Comparison of theoretical paths and data can be done using charts or with a computer program that carries out the best fit. The advantage of using charts is that they can easily be employed in the field.

3.1. Theoretical α-β-L/T paths

The following analysis is based on the deformation at an isolated single straight fault in an otherwise homogenously deforming medium. The fault is supposed to have a limited extent, so that the offset reduces to zero at both ends. We consider a plane-strain case, with the fault oriented parallel to the intermediate principal stretching direction. The problem can therefore be regarded as two-dimensional. If deformation is not plane strain, stretching or shortening in the third dimension would cause an area change in the section under consideration, but no changes in the angles and other parameters that are used below. We further consider an initially straight foliation perpendicular to the section under consideration.

Similar to Kocher and Mancktelow (2005), we fix our reference frame to be parallel and perpendicular to the far-field foliation orientation. The foliation is assumed

to be one of the flow eigenvectors or apophyses (Passchier, 1988; Ebner and Grasemann, 2006). The bulk flow field is now given by the position gradient tensor **F**:

$$\mathbf{F} = \begin{pmatrix} a & g \\ 0 & 1/a \end{pmatrix}, \tag{1}$$

where a is the amount of stretching, and g the amount of shearing, both parallel to the foliation. Because of the definition of the reference frame, the far field foliation does not rotate relative to the reference frame, but it may stretch or shorten if $a \neq 1$. **F** is area-conservative because of our assumption of plane-strain flow.

It is also assumed that the fault is frictionless, so that it cannot support any shear stress. This implies that the material adjacent to the fault stretches/shortens in pure shear parallel to the fault. Rotation of the fault adds a spin to the deformation, but deformation immediately adjacent to the fault plane remains coaxial. Furthermore, the fault as a whole behaves as a passive plane, or a line in 2D, and therefore stretches and shortens according to the bulk flow field. We define e as the amount of stretching or longitudinal strain of the fault (its finite length / original length). With these assumptions an analytical solution exists for the evolution of α, β and L/T for a layer that intersects the fault at its centre.

To determine the orientation of the fault with progressive strain, we consider a unit vector parallel to the fault. This vector has initial coordinates $[\cos(\alpha_0),\sin(\alpha_0)]$. After deformation, and due to the application of the tensor **F**, the vector will have new coordinates $[a\cdot\cos(\alpha_0)+g\cdot\sin(\alpha_0),(1/a)\cdot\sin(\alpha_0)]$. The stretching ($e$), parallel to the fault, is the ratio of the finite and original length of the unit vector:

$$e = \sqrt{\left(a\cdot\cos(\alpha_0)+g\cdot\sin(\alpha_0)\right)^2 + \frac{1}{a^2}\sin^2(\alpha_0)}. \tag{2}$$

The finite orientation (α) of the fault relative to foliation is:

$$\alpha = \arctan\left(\frac{\sin(\alpha_0)}{a^2\cdot\cos(\alpha_0)+a\cdot g\cdot\sin(\alpha_0)}\right). \tag{3}$$

As deformation progresses the foliation is reoriented at the fault, describing a drag angle (β) between the foliation and the fault plane. We use the assumption of a frictionless fault and therefore pure shear parallel to the fault. The foliation at the fault thus experiences a stretching (e) parallel to the fault, while it passively rotates along with the fault. Stretching and rotation determine the drag angle. A local position gradient (**F'**) tensor can be defined in a coordinate system parallel to the fault:

$$\mathbf{F'} = \begin{pmatrix} e & 0 \\ 0 & 1/e \end{pmatrix}. \tag{4}$$

A unit vector in this local coordinate system will change from initial coordinates $[\cos(\beta_0),\sin(\beta_0)]$ to new coordinates $[e\cdot\cos(\beta_0),(1/e)\cdot\sin(\beta_0)]$. The angle ($\beta$) between foliation at the fault and that fault will then be (using $\alpha_0 = \beta_0$):

$$\beta = \arctan\left(\frac{\sin(\beta_0)}{e^2\cdot\cos(\beta_0)}\right) = \arctan\left(\frac{\sin(a_0)}{e^2\cdot\cos(a_0)}\right). \tag{5}$$

The reference layer should intersect the fault just at the centre of it, where the maximum displacement can be found. Away from the fault the finite thickness (T) of that layer is a function of the bulk finite strain and its original thickness (T_0):

$$T = \frac{T_0}{a} \tag{6}$$

The initial fault-parallel thickness (L_0) is:

$$L_0 = \frac{T_0}{\sin(\alpha_0)}. \tag{7}$$

This line L_0 gets stretched by the same amount (e) as the fault, so its length after deformation will be:

$$L = e\cdot L_0 = \frac{e\cdot T_0}{\sin(\alpha_0)} \tag{8}$$

As the absolute dimensions are irrelevant for the geometry of the system, we combine equation (7) and (8) to obtain the ratio L/T:

$$L/T = \frac{e \cdot T_0}{\sin(\alpha_0)} \frac{a}{T_0} = \frac{e \cdot a}{\sin(\alpha_0)} \quad (9)$$

We now have the three measurable parameters α, β and L/T as a function of the unknown variables α_0, a, and g. Although the combination of a and g defines the amount of finite strain and the kinematics of strain, it may be more useful to use the two variables finite strain ration (R_f) and vorticity angle (ω) or vorticity number (Wk). R_f is the axial ratio of the finite strain ellipse and ω the angle between the flow apophyses, with:

$$\omega = \arctan\left(\frac{a - 1/a}{g}\right), \; Wk = \cos(\omega) \quad (10)$$

and

$$R_f = \frac{2\sqrt{g^2 + \frac{1}{4}\left(1/a + a\right)^2} + \sqrt{g^2 + \left(a - 1/a\right)^2}}{2\sqrt{g^2 + \frac{1}{4}\left(1/a + a\right)^2} - \sqrt{g^2 + \left(a - 1/a\right)^2}} \quad (11)$$

ω can range from 0° for simple shear (Wk=1) to +90° for pure shear (Wk=0) stretching parallel to the foliation, or -90° for pure shear shortening parallel to the foliation.

With the above equations, curves of α and L/T as a function of β are shown for different vorticity angles and starting orientation of the fault (Fig. 5).

3.2. Determining vorticity and initial fault angle with charts

To determine the vorticity (ω) and initial fault orientation (α_0), α, β and L/T need to be measured on a population of faults with drag folds. Such data can be measured in the field or from pictures. The plane of observation should be perpendicular to both fault and foliation. If not, the apparent values should be corrected to get the true values. The data should be collected as close as possible to the middle of the fault, so that equation (2) holds for the stretching of the material immediately adjacent to the fault. It should also be noted that these equations can be only used when the fault is discrete. In case of a narrow ductile shear band, the angle β would be modified due to shearing of the foliation in the narrow zone (Fig. 1b).

Applying the above equations, several unique graphs for the evolution of α', β and L/T can be plotted for progressive strain, for a certain starting orientation of the fault (α_0) and a certain vorticity angle (ω) (Fig 5). Charts covering the full range of ω from -90 to +90° and α_0 from 0 to 180° are provided in the appendix. We assume that all the shear bands start off at different times, but with a similar orientation. Each fault then represents a different stage of development. The data can be plotted in each of the graphs of figure 5. Ideally, all data should plot on a single curve that represents the evolution of a fault system with a certain α_0 and ω. The fault that experienced the least strain should lie closest to the estimated initial fault angle (α_0). The total amount of strain can be estimated from that for the most developed fault system. This is, of course, a minimum estimate, because even the most developed, oldest fault that is found must not necessarily have experienced the total finite strain of the host rock. The pair of curves in figure 5 that best fits the eight measurements is the one for ω=0° (simple shear) and α_0 is 70° to 80°. The highest strain the rock experienced is estimated to be between R_f=8 and 16, which corresponds to a dextral shear strain of 2.47 to 3.76.

Figure 5 shows that the curves for different α_0 and ω are distinct, as long as α_0 is larger than about 40°. This means that the method is only applicable to faults that started off at a high angle to the foliation.

3.3. Numerical implementation of the method

Finding the curve that best fits the data can also be done numerically, using a least-squares approach. A small program that does the curve fitting was written in the language "C" (source code can be obtained from the authors). Input is a text file containing a list of α, β and L/T data. The program cycles through all possible vorticity angles (-90° to +90°) and α_0 angles (0 to 180°), each with increments of 1°. For each ω and α_0 combination, the program then calculates the α-β-L/T curve for progressive strain, increasing strain in small increments. For each strain increment and each i-th data point, the difference Δ_i between the theoretical and measured α, β, L/T values is calculated:

$$\Delta_{i(\alpha_0,\omega,Rf)} = \sqrt{\left(\alpha_c - \alpha_i\right)^2 + \left(\beta_c - \beta_i\right)^2 + w\left(L/T_c - L/T_i\right)^2} \qquad (12)$$

Here the subscript c stands for theoretical values and i for measured data. Because the range of L/T values differs from that of the angles α and β, L/T data may be given a different weighting (w) for the least-squares best fit. For a given ω and α_0 combination, the sum ($\Sigma\Delta_i$) of the smallest Δ_i-value for each data point is a measure of how well that ω and α_0 combination fits the data. The ω and α_0 combination with the lowest $\Sigma\Delta_i$ is regarded as the best estimate of ω and α_0. Once a best estimate for ω and α_0 is found, one can estimate the amount of strain that each analysed fault experienced by finding the strain that minimises Δ_i, using equation (12).

4. Validation of the method

4.1. Introduction

In order to ascertain the validity of the method, it has been tested on several analogue and numerical experiments with different initial fault angles and different boundary conditions. First, the method has been applied to a simple shear analogue model from Exner et al. (2004) and later to a pure shear experiment of our own. We also ran a series of numerical experiments with a variety of initial angles and vorticities, ranging from pure to simple shear. In all cases, we measured α, β and L/T of a single drag fold structure at different stages of its development, and applied the least-squares best-fit routine to the data.

4.2. Validation on a simple shear analogue experiment

Exner et al. (2004) studied drag fold structures at a fault in a deforming a homogeneous, linear viscous matrix material (PDMS) in a ring shear rig. Each of their models started with a predefined fault, lubricated using liquid soap and silicone oil. They tracked the offset and deflection of foliation around the fault using a marker grid. We used published images of one experiment for α_0=90° according to the authors (Fig 6, after their figure 6). It should be noted that the actual starting angle in that experiment was slightly less, about 87°. The fault initially has antithetic slip and develops reverse drag folds. At a shear strain of 2.3, the fault has rotated 67° and slip reverses to become synthetic. In the terminology of Grasemann et al. (2003) the system evolves from a reverse-drag a-type, to a normal-drag s-type flanking fold.

Nine groups of data (α, β, L/T) were measured from the figures of Exner et al. (2004) up to a shear strain of 1.8, where the finite offset along the fault is still antithetic. With our analysis (Fig. 7) we obtained an estimated initial fault angle of 85° (true value 87°) and a vorticity angle of ω=3° or Wk=1.00 (true value 0° and 1.00 respectively).

4.3. Validation on pure shear analogue experiments

To test the method on a pure shear case, we used the deformation apparatus described by Carreras and Ortuño (1990) and Druguet and Carreras (2006). The deforming medium was soft, commercially available plasticine. This material has been characterized as non-linear elasto-viscous with a stress exponent of 3, an effective viscosity η~$4 \cdot 10^7$ Pa·s at the experimental conditions, a density ρ of $1.15 \cdot 10^3$ kg/m^3, and shear modulus G~10^5 Pa (Gomez-Rivas, 2005). The model had initial dimensions of 29x15x10 cm and was deformed in pure shear at a temperature of 26ºC and at a strain rate of $4 \cdot 10^{-5}$ s^{-1}. Since tests with a lubricated cut, as used by Exner et al. (2004), failed, we simulated the fault with a lenticular fracture that was filled with much softer PDMS (Fig. 8). The fault was initially oriented 60° to the extension direction. A 5 mm grid was drawn on the surface of the plasticine. Plane-strain pure-shear deformation was applied by moving the sides of the sample, while keeping the sample thickness constant at 10 cm.

Shortening lead to a rotation of the fault and the development of reverse-drag folds. The soft PDMS was squeezed towards the tips of the fault, where wing cracks developed. Despite these developments, our analysis of six data groups, measured every 10% shortening, gave a good estimate of the vorticity (89° instead of 90°) and initial fault angle (59° instead of 60°) (Fig. 9).

4.4. Validation on finite element numerical simulations

As shown above, our proposed method appears to work well for ideal pure and simple shear deformation. Unfortunately, experimental data were not available for general shear. We therefore conducted a series of finite element models to test the method for a range of vorticities and initial fault angles. For the numerical simulations we used the code BASIL (Barr and Houseman, 1996) that is linked to the modelling platform Elle (Jessell et al., 2001).

The models were two-dimensional and consisted of a square containing a narrow ellipse in the centre (Fig. 10). The host rock was simulated with a homogeneous isotropic linear viscous material with a viscosity (η) of one. A single layer of viscosity 1.1 represented the foliation in the host rock. Like Grasemann and Stüwe (2003) we simulated the fault in the centre of each model with a narrow ellipse with a viscosity of 0.01. Two types of initial geometries were considered, with the ellipse oriented at 45º and 75º to the foliation, respectively. These two models were deformed under different velocity boundary conditions, from simple to pure shear, varying the vorticity angle (ω) by 30º (Table 1). The grid was generated with a self-meshing routine using Delauney triangles with a minimum angle of 10º.

At least 6 groups of data (α, β, L/T) were measured at different finite strain from each simulation, and analyzed to determine the vorticity and initial fault angle. The difference between true and estimated values are plotted in Fig. 11, and listed in table 1.

Differences in Wk ranges from 0 to 0.1 at the most, and estimated initial fault angles are within 7º of the true values.

Summarizing, in all tests the results from the analysis closely match the known true values of the physical and numerical experiments, allowing us to apply the method to naturally deformed rocks with confidence.

5. Strain analysis applied to the Mas Rabassers de Dalt outcrop

A total of 29 small antithetic faults in the quartzite layer at Mas Rabassers de Dalt (Fig. 3) were analyzed to estimate the deformation experienced by this rock. The finite fault orientations ranged from α=10 to 64° (Table 2). The data were processed with the software described in section 3.3. The results showed an initial fault angle (α_0) of 78º and a vorticity angle (ω) of 3º, which gives a vorticity (Wk) of 1.00 (dextral simple shear). The highest strain was recorded by fault structure number 5 (at locality C in Fig. 3) with a finite strain of about Rf=8 to 16, which is equivalent to a shear strain of about 2.47 to 3.76.

The dextral simple shear inferred from this analysis is consistent with the field observations: the quartzite layer is oriented parallel to the zone of highest D3 shear strain. Only one small fault (locality F) was found away from the main shear zone, but this one, with a high angle of α=54° to the foliation, experienced less finite shear strain.

The available data set it is large enough to test the precision of the method. This was done by randomly selecting subsets of 5, 9, 13, 17, 21 and 25 data and using these subsets to determine vorticity and initial fault angle. Ten different random subsets were processed for each size of the subset. Figure 13 shows that even very small datasets (5 to 9 data) already give approximately the right solution. It should also be noted that least-squares best fit using 29 data points (measured by EGR) produced almost identical results to that using the graphs (Fig. 5) on only eight data points independently collected by someone else (PDB). This not only indicates that the graphical method with a limited data set produces good results but also that user bias does not seem to be a significant factor in the analysis.

6. Discussion and conclusions

In this paper we have shown that small-scale faults with drag folds can be used to determine vorticity, initial fault angle, and estimate of the minimum finite strain since first fault nucleation. This is a useful addition to the structural geologist's "toolbox" because relatively few methods exist to determine and quantify vorticity (Ghosh, 1987; Passchier and Urai, 1988; Wallis, 1992; Short and Johnson, 2006).

The initial fault angle (α_0) can usually be estimated in the field, by finding the steepest fault with the least offset and drag fold bending. If this α_0 is determined independently first, it can of course be used in the subsequent determination of the vorticity angle (ω), either when using the graphs (Fig. 5 and Appendix), or when using the least-squares technique. In the latter case one can set α_0 and only iterate over ω and Rf to find the best fit. However, without using a priori knowledge of α_0, the method appears robust and produced estimated values close (<10°) to the true ones in all tests on experiments and numerical simulations.

In the field study with 29 measured faults, simple shear deformation was obtained, which is consistent with the known local deformation at Mas Rabassers de Dalt. Still, one cannot determine the exact vorticity that the quartzite experienced with only orientations of foliations, fold axes, and other structural elements. Local field

observations made so far only indicated a dominant simple shear component, leaving open sub-simple shear with some shortening or stretching parallel to the shear plane. With the new analysis of the faults with drag folds the vorticity is better constrained.

In conclusion, we propose a new method to determine vorticity, initial fault angle and finite strain using small-scale faults with drag folds. Theory and validation tests on experiments and numerical simulations show that the method is robust, provided the following assumptions hold: (a) the structures nucleate at different stages during deformation, and therefore record different amounts of strain, (b) the faults all nucleate in approximately the same orientation (α_0), (c) the flow kinematics do not change during deformation, (d) the structures are isolated to avoid interference between adjacent structures, and (e) the faults are discrete, so that the drag angle (β) can be determined accurately. The last assumption means that ductile shear bands (Fig. 1b) are not suitable for this method.

Although a least-squares best fit routine is preferred to obtain the best estimate of vorticity, initial fault angle and minimum finite strain, charts can be used to obtain a first estimate.

Acknowledgements

This work was financed through the PhD grant BES-2003-0755 to EGR and research project CGL2004-03657, both funded by the Spanish Ministry of Education and Science. We thank Jens Becker and Anne Peschler for their help with the BASIL modelling.

Appendix A. Charts to estimate initial fault angle (α_0), vorticity (ω) and minimum finite strain (Rf)

To use these charts, measure the following parameters from a number of fault systems, preferably at different stages of development (Fig. A1):

- The angle between the fault and the foliation away from the fault (α);
- The angle between the fault and the deflected foliation at the fault (β);
- The ratio (L/T) of the thickness of a layer away from the fault (T) and the thickness of the same layer parallel to the fault and at the fault (L).

Each pair of graphs is for a certain vorticity, defined by the angle between the flow apophyses (ω) or the vorticity number (Wk). Arrows in the graphs show α-β (left) and L/T-β (right) paths as a function of increasing finite strain and initial fault orientation (α_0). Dashed lines are finite strain contours at Rf = 2, 4, 8, and 16.

Plot your measurements on a transparency, using the blank pair of graphs provided (Fig. A2). Then overlay your plot on the graphs (Figs. A3 to A6) and find the vorticity where your data most closely follow one single arrow on both graphs. The arrow fitting your data points provides you with the starting orientation of the faults. Ideally, each data point should have the same finite strain in both graphs as well.

References

Barnolas, A. and Chiron, J. C. 1996. Synthèse géologique et géophysique des Pyrénées. BRGM-ITGE. 729 pp.

Barr, T. D. and Houseman, G. 1996. Deformation fields around a fault embedded in a non-linear ductile medium. Geophysical Journal International 125, 473-490.

Bons, P. D., Druguet, E., Hamann, I., Carreras, J. and Passchier, C. W. 2004. Apparent boudinage in dykes. Journal of Structural Geology 26, 625-636.

Carreras, J. 2001. Zooming on Northern Cap de Creus shear zones. Journal of Structural Geology 23, 1457-1486.

Carreras, J. and Casas, J. M. 1987. On folding and shear zone-development: a mesoscale structural study on the transition between two different tectonic styles. Tectonophysics 135, 87-98.

Carreras, J., Druguet, E. and Griera, A. 2005. Shear zone-related folds. Journal of Structural Geology 27, 1229-1251.

Carreras, J. and Ortuño, F. 1990. Fundamento geométrico y cinemática de la modelización teórica y experimental de deformaciones no-coaxiales. Acta Geológica Hispánica 17, 219-225.

Coelho, S., Passchier , C. W. and Grasemann, B. 2005. Geometric description of flanking structures. Journal of Structural Geology 27, 597-606.

Druguet, E. 1997. The structure of the NE Cap de Creus Peninsula. Unpublished PhD thesis. Universitat Autònoma de Barcelona.

Druguet, E. 2001. Development of high thermal gradients by coeval transpression and magmatism during the variscan orogeny: Insights from the cap de creus (Eastern Pyrenees). Tectonophysics 332, 275-293.

Druguet, E. and Carreras, J. 2006. Analogue modelling of syntectonic leucosomes in migmatitic schists. Journal of Structural Geology 28, 1734-1747.

Druguet, E. and Hutton, D. H. W. 1998. Syntectonic anatexis and magmatism in a mid-crustal transpressional shear zone: an example from the Hercynian rocks of the eastern Pyrenees. Journal of Structural Geology 20, 905-916.

Druguet, E., Passchier, C. W., Carreras, J., Victor, P. and Den Brok, S. 1997. Analysis of a complex high-strain zone at Cap de Creus, Spain. Tectonophysics 280, 31-45.

Ebner, M. and Grasemann, B. 2006. Divergent and convergent non-isochoric deformation. Journal of Structural Geology 28, 1725-1733.

Exner, U., Mancktelow, N. S. and Grasemann, B. 2004. Progressive development of s-type flanking folds in simple shear. Journal of Structural Geology 26, 2191–2201.

Fusseis, F., Handy, M. R. and Schrank, C. 2006. Networking of shear zones at the brittle-to-viscous transition (Cap de Creus, NE Spain). Journal of Structural Geology 28, 1228-1243.

Gayer, R. A., Powell, D. B. and Stephen, R. 1978. Deformation against metadolerite dykes in the Caledonides of Finnmark, Norway. Tectonophysics 46, 99-115.

Gomez-Rivas, E. 2005. Shear bands en materiales anisótropos: modelización analógica en condiciones de deformación coaxial. Unpublished MSc thesis. Universitat Autònoma de Barcelona.

Ghosh, S. K. 1987. Measure of non-coaxiality. Journal of Structural Geology 9, 111-114.

Grasemann, B., Martel, S. and Passchier, C. 2005. Reverse and normal drag along a fault. Journal of Structural Geology 27(6), 999-1010.

Grasemann, B. and Stuwe, K. 2001. The development of flanking folds during simple shear and their use as kinematic indicators. Journal of Structural Geology 23(4), 715-724.

Grasemann, B., Stüwe, K. and Vannay, J.-C. 2003. Sense and non-sense of shear in flanking structures. Journal of Structural Geology 25, 19-34.

Harris, L. B. 2003. Folding in high-grade rocks due to back-rotation between ductile shear zones. Journal of Structural Geology 25, 223-240.

Harris, L. B., Koyi, H. A. and Fossen, H. 2002. Mechanisms for folding of high-grade rocks in extensional tectonic settings. Earth Science Reviews 59, 163-210.

Hudleston, P. J. 1989. The association of folds and veins in shear zones. Journal of Structural Geology 11, 949-957.

Jessell, M., Bons, P. D., Evans, L., Barr, T. and Stüwe, K. 2001. Elle: the numerical simulation of metamorphic and deformation microstructures. Computers and Geosciences 27, 17-30.

Kocher, T. and Mancktelow, N. S. 2005. Dynamic reverse modelling of flanking structures: a source of quantitative kinematic information. Journal of Structural Geology 27, 1346-1354.

Kocher, T. and Mancktelow, N. S. 2006. Flanking structure development in anisotropic viscous rock. Journal of Structural Geology 28, 1139-1145.

Koyi, H. A. and Skelton, A. 2001. Centrifuge modelling of the evolution of low-angle detachment faults from high-angle normal faults. Journal of Structural Geology 23, 1179–1185.

Odonne, F. 1990. The control of deformation intensity around a fault: natural and experimental examples. Journal of Structural Geology 12, 911–921.

Passchier , C. W. 1998. Monoclinic model shear zones. Journal of Structural Geology 20, 1121-1137.

Passchier, C. W. 2001. Flanking structures. Journal of Structural Geology 23, 951-962.

Passchier, C. W. and Urai , J. L. 1988. Vorticity and strain analysis using Mohr diagrams. Journal of Structural Geology 10, 755-763.

Ramsay, J. F. and Huber, M. I. 1983. The techniques of modern structural geology. Academic Press, London.

Schmid, D. W. and Podladchikov, Y. Y. 2003. Analytical solutions for deformable elliptical inclusions in general shear. Geophysical Journal International 155, 269-288.

Short, H. A. and Johnson, S. E. 2006. Estimation of vorticity from fibrous calcite veins, central Maine, USA. Journal of Structural Geology 28, 1167-1182.

Wallis, S. R. 1992. Vorticity analysis in a metachert from the Sanbagawa belt, SW Japan. Journal of Structural Geology 14, 271-280.

Wiesmayr, G. and Grasemann, B. 2005. Sense and non-sense of shear in flanking structures with layer-parallel shortening: implications for fault-related folds. Journal of Structural Geology 27, 249-264.

Figure captions

Fig. 1. Schematic illustration of the formation of reverse-drag folds adjacent to (a) isolated faults and (b) shear bands in a general shear field (W_k=0.64) that is homogeneous far away from the fault/shear band. In case of a ductile shear band, normal drag is found within the shear band, in addition to reverse drag away from the shear band. The same applies to antithetic movement (top) and to synthetic movement (bottom). Left column shows the geometry before deformation.

Fig. 2. Drag fold structures in the banded quartzite at Mas Rabassers de Dalt, Cap de Creus, Spain. Sense of shear is top (east) to the right. (a-b) Antithetic faults with reverse-drag folds at different stages of development. (c) One of the rare synthetic

faults. (d) Photograph and sketch showing that in the third dimension the faults are straight and extend further than their length perpendicular to the banding. (e) Plane-polarised light micrograph of an antithetic fault. Variations in the content of graphite and mica particles form the dark and light bands. (f) Same image in cross-polarised light. Quartz grain size is largest in clean quartz. All images looking onto the surface perpendicular to the foliation and faults. Black scale bars 10 mm, white scale bars 0.5 mm, Ø of 5 €-cent coin is 21 mm.

Fig. 3. Detailed map of the Mas Rabassers de Dalt Outcrop showing the refolded quartzite bed and the localities where the small-scale faults were found and measured. The stereoplot summarizes the main structural information: poles to quartzite bedding (open dots) that lie on great circle (dashed line) defining the D_3 fold axis (closed dot) which lies on the great circle of the average D_3 shear plane. The cross is the average D_3 shear direction. (Based on Druguet, 1997).

Fig. 4. Sketch showing a fault and drag fold in the undeformed (a) and deformed (b) stage, with all the parameters that are required for the analysis.

Fig. 5. Curves of α and L/T as a function of β for different vorticity angles and starting orientations of the fault. This chart can be used to estimate Rf, vorticity and initial fault angle in the field. Insets show the Mohr-circle for stretch for an R_f-value of 4. Eight data points from Rabassers de Dalt are plotted in each of the graphs. The pair of curves that best fits these data is the one for ω=0° (simple shear) and α_0 is between 70º and 80°. The highest strain the rock experienced is estimated to be between R_f=8 to 16 (shear strain is 2.47 to 3.76).

Fig. 6. Progressive development of a reverse a-type flanking fold (Modified from Exner et al. (2004).

Fig. 7. Curves of α, β and L/T for simple shear and a starting orientation of the fault of 85º, which best fit the data measured from the experiment of Exner et al. (2004).

Fig. 8. Initial and final stage of a pure shear analogue model showing the evolution of an pre-existing fault (a PDMS-filled lens) and its associated drag folds. The side of each square is 0,5 cm. wide.

Fig. 9. Curves of α, β and L/T for pure shear and a starting orientation of the fault of 59º. The measured data points of our experiment fit precisely to the calculated curves.

Fig. 10. (a) Initial configuration in finite element simulations with BASIL for an initial fault angle of 75º. (b) Geometry at the end of a simulation for Wk=0.5 at a finite strain of Rf=2.6.

Fig. 11. Comparison of true (open dots) and estimated (closed dots) values of vorticity number and initial fault angles, for eight numerical simulations with BASIL.

Fig. 12. Curves of α, β and L/T for a vorticity angle of 3º and an initial fault angle of 78º. The plotted data correspond to the measured parameters at Mas Rabassers de Dalt.

634 Fig. 13. Graph showing the stability of this analytical method using a different number
635 of groups of measurements. The solution becomes stable using less than 10 groups of
636 data.
637
638 Fig. A1. Definition of parameters.
639
640 Fig. A2. Plot your data on a transparency using these blank charts.
641
642 Fig. A3 to A6. Curves of α and L/T as a function of β for different vorticity angles (ω)
643 and starting orientations of the fault (α_0). Insets show the Mohr-circle for stretch for an
644 R_f-value of 4. Dashed lines are finite strain contours at $Rf = 2$, 4, 8, and 16.
645
646 **Tables**
647
648 Table 1. True and calculated values of vorticity (Wk) and initial fault angle (α_0) for
649 eight finite element simulations, showing that errors in Wk are below 0.1 and in α_0
650 below 7º.
651
652 Table 2. Values of α, β and L/T measured from the Rabassers de Dalt outcrop.
653 Localities are indicated on the outcrop map (Fig. 3).
654

Figure1
Click here to download high resolution image

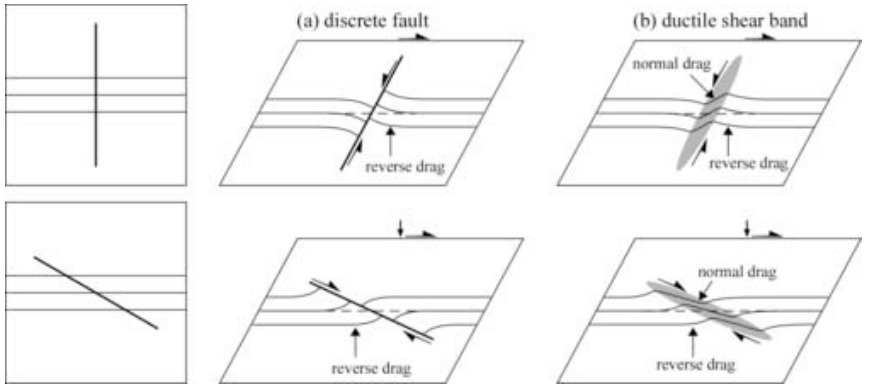

Figure2
Click here to download high resolution image

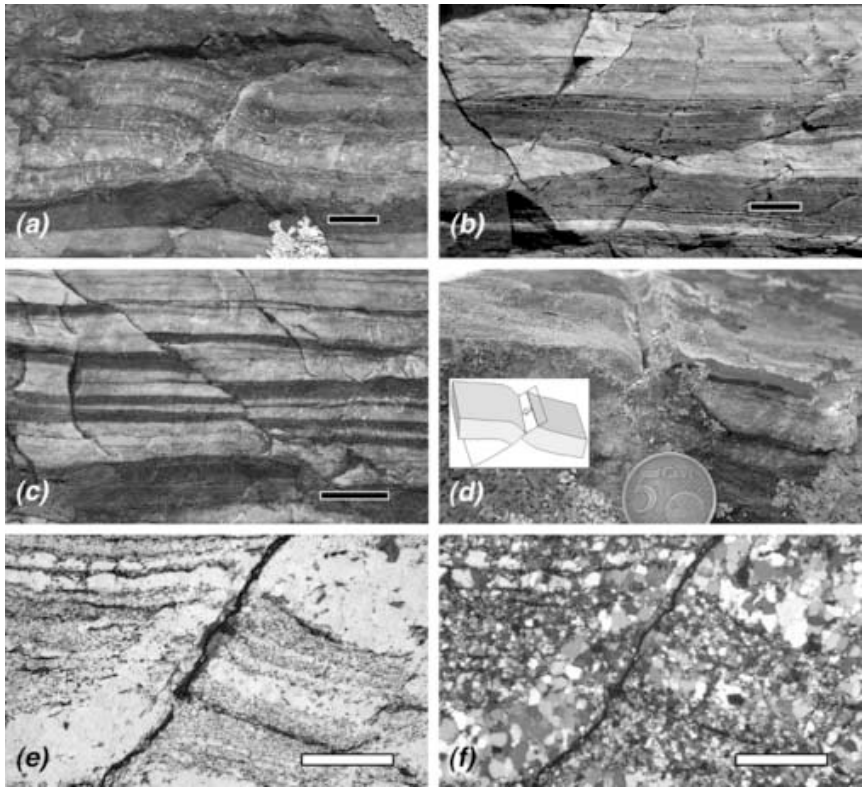

Figure3
Click here to download high resolution image

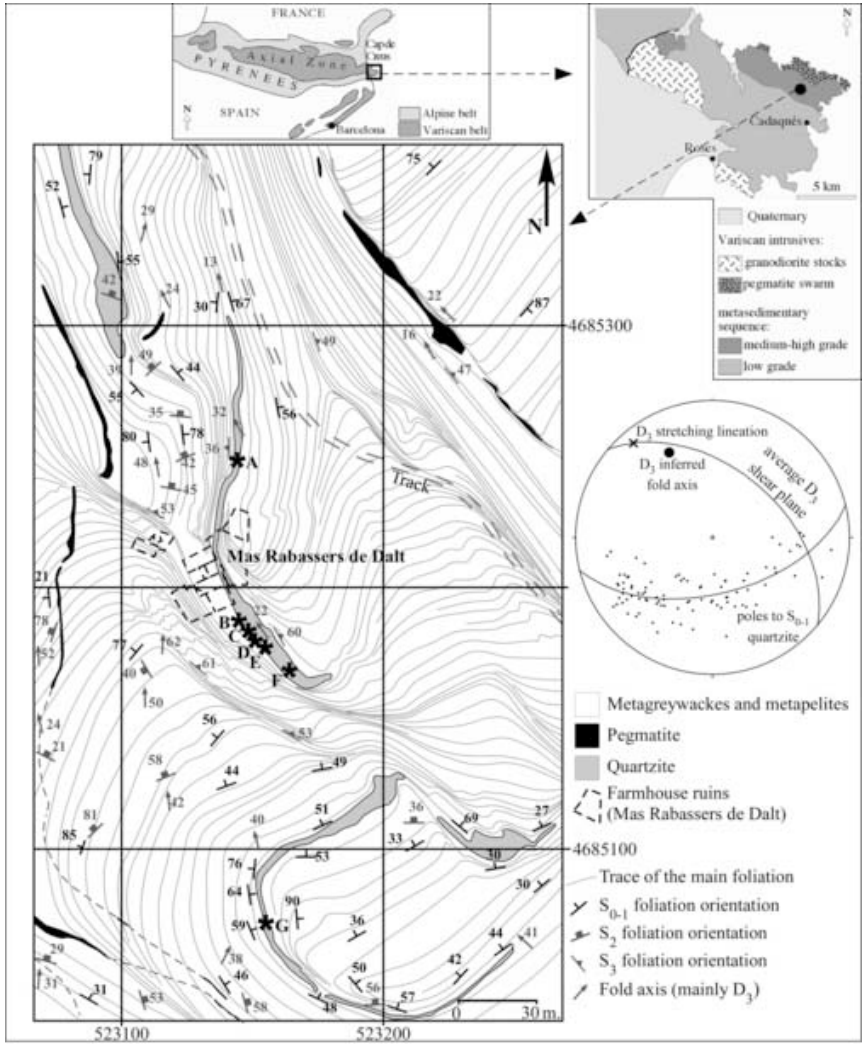

Figure4
Click here to download high resolution image

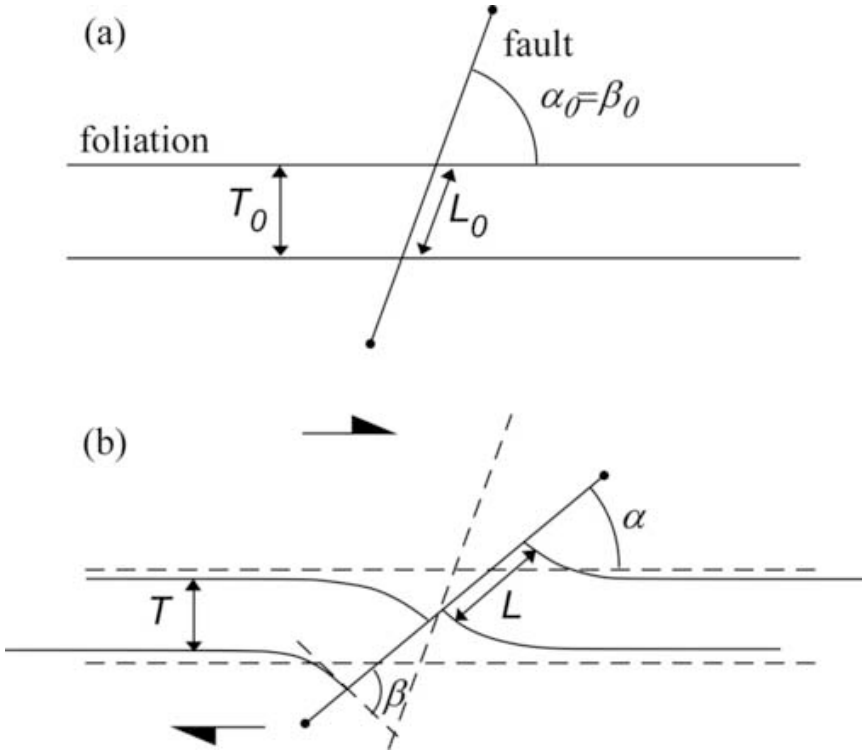

Figure5
Click here to download high resolution image

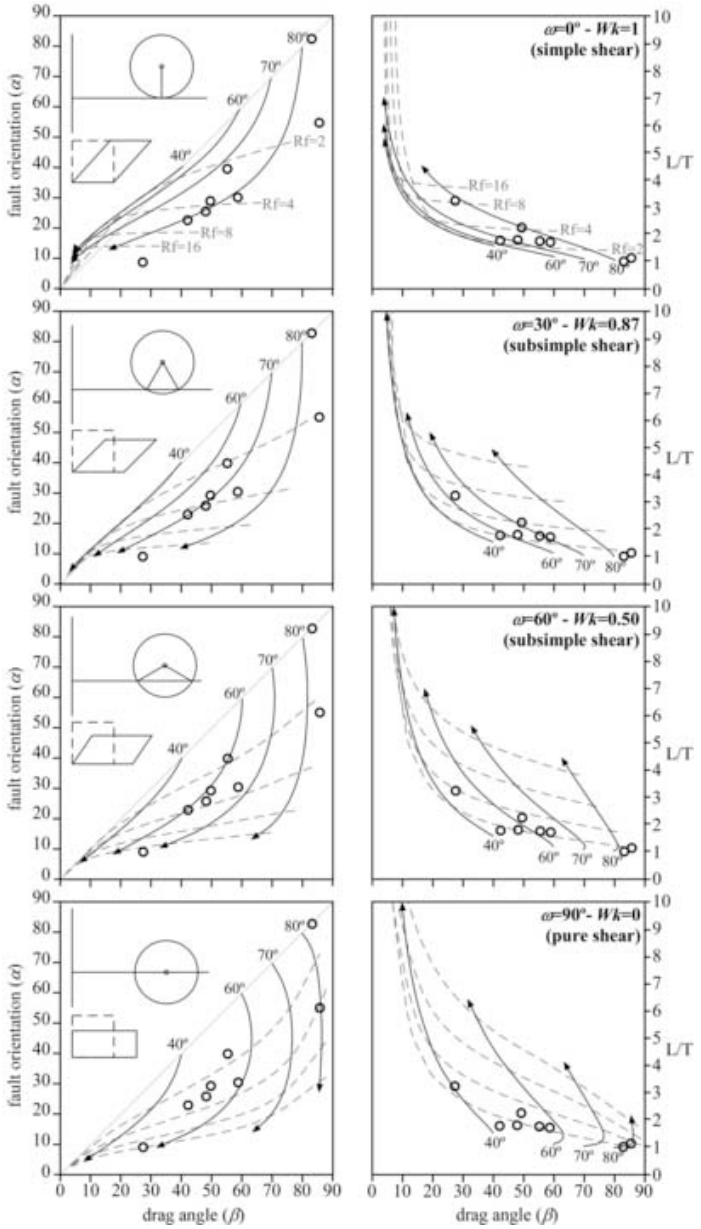

Figure6
Click here to download high resolution image

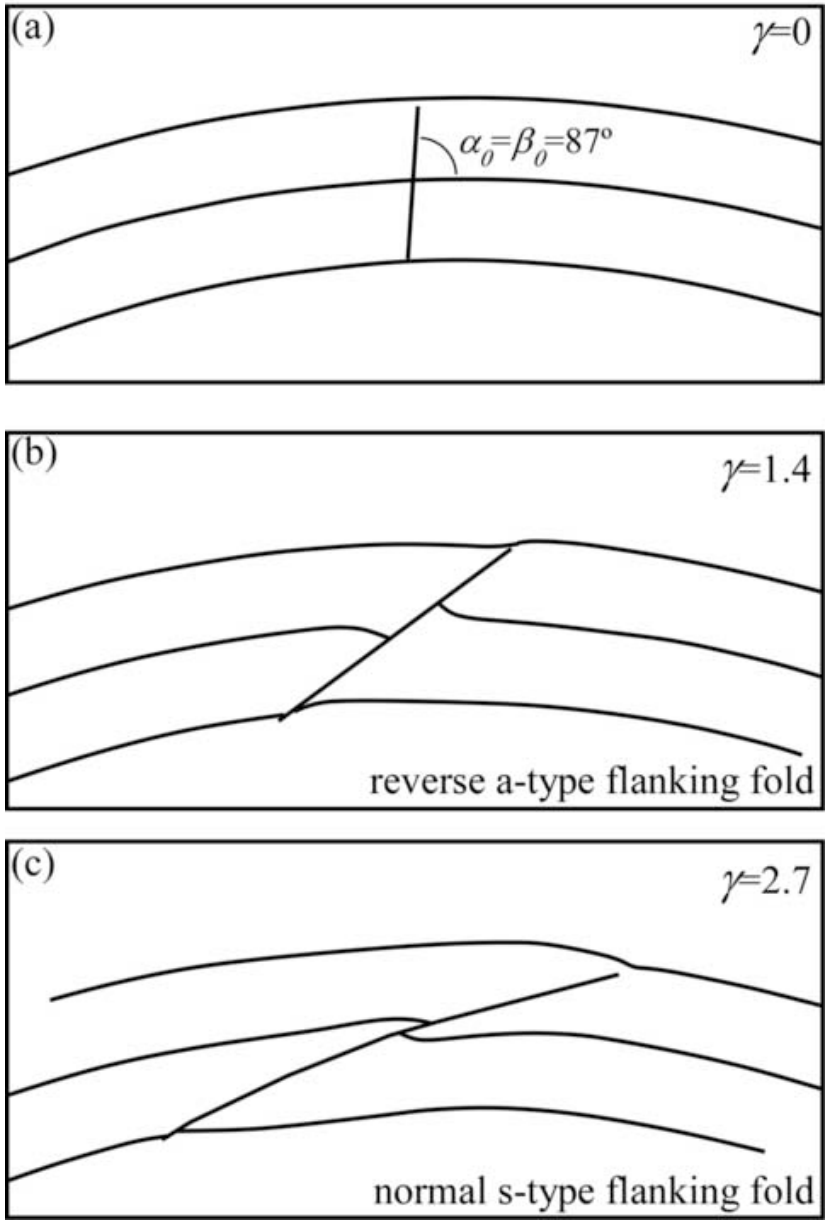

Figure7
Click here to download high resolution image

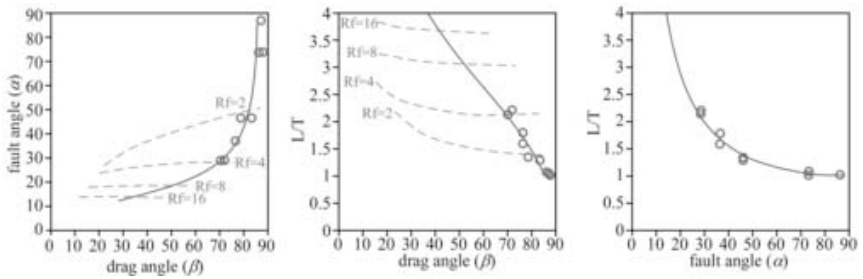

Figure8
Click here to download high resolution image

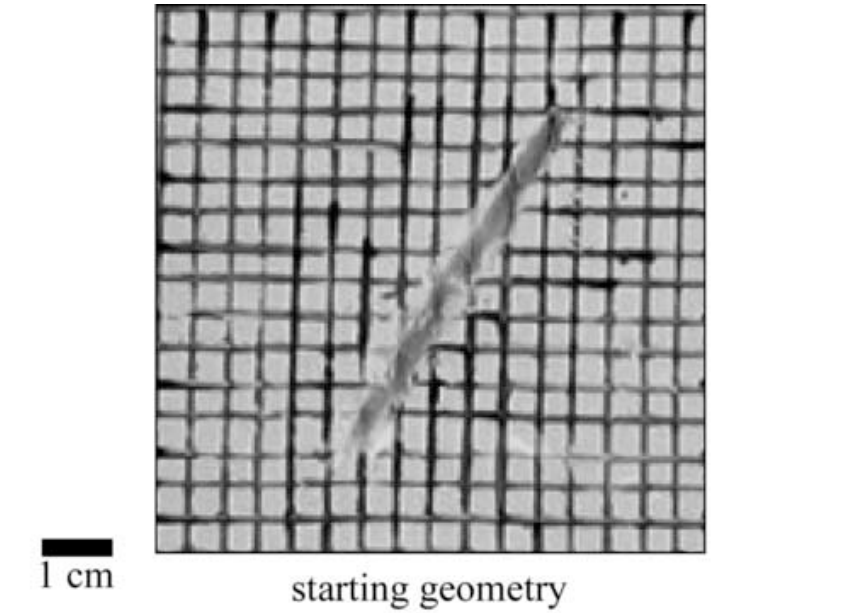

Figure9
Click here to download high resolution image

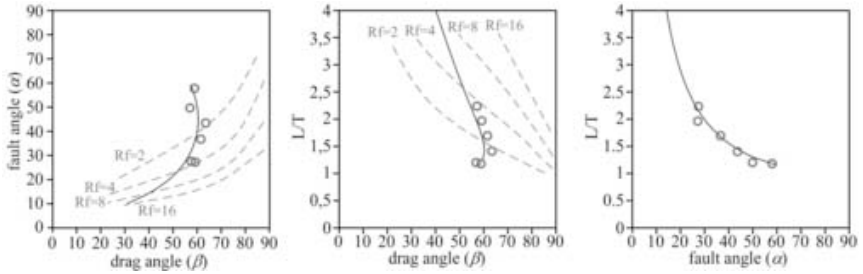

Figure10
Click here to download high resolution image

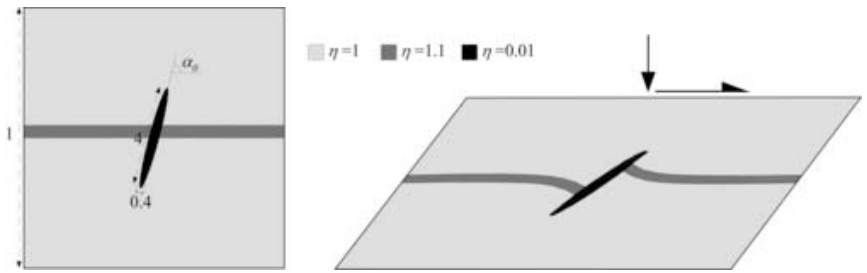

Figure11
Click here to download high resolution image

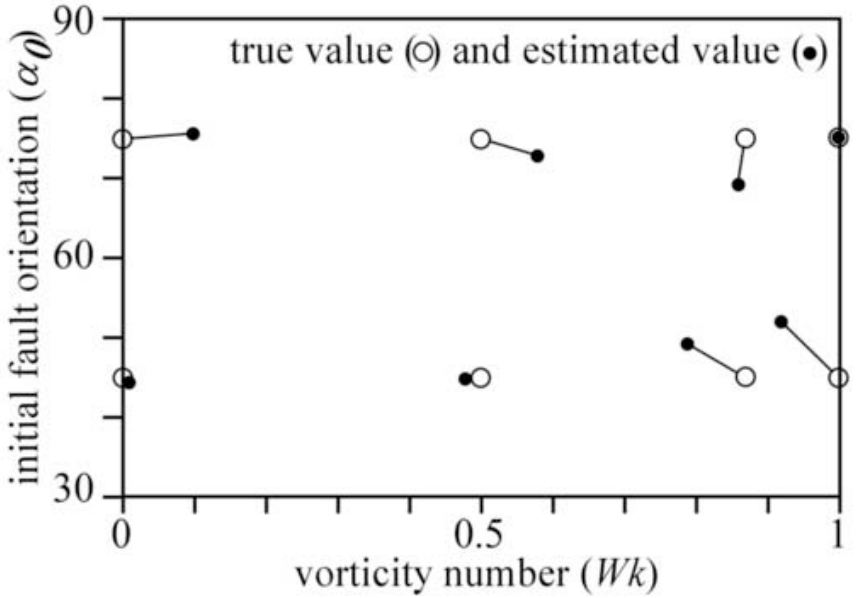

Figure12
Click here to download high resolution image

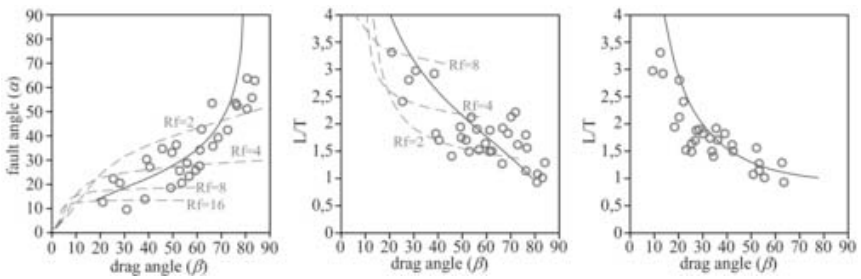

Figure13
Click here to download high resolution image

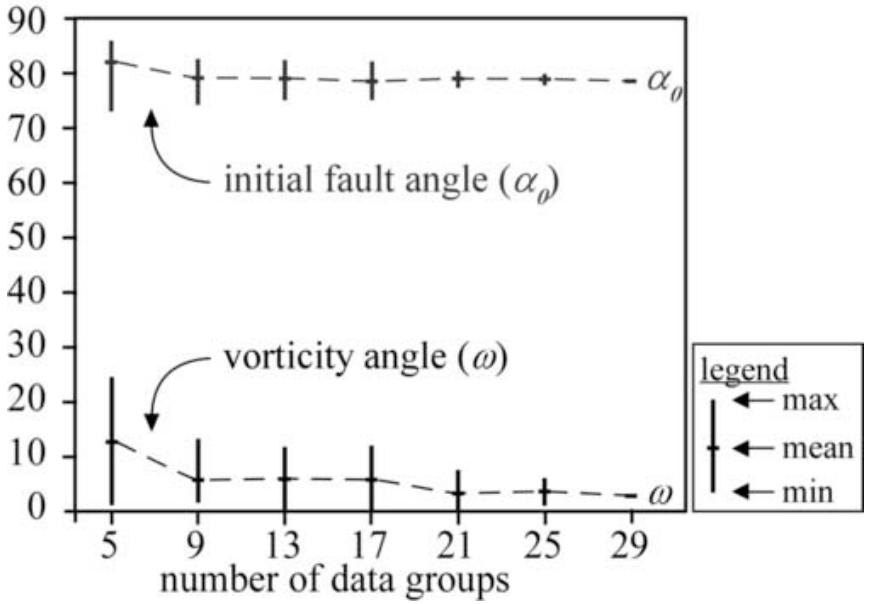

FigureA1
Click here to download high resolution image

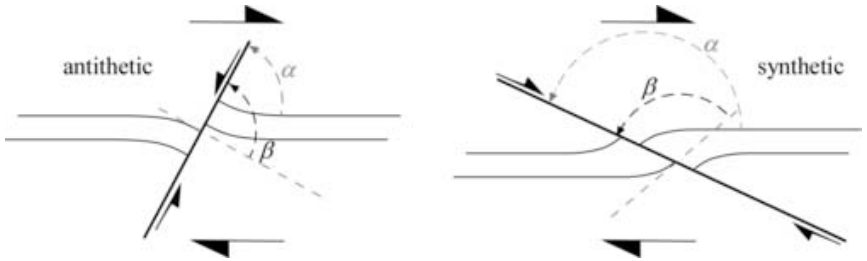

FigureA2
Click here to download high resolution image

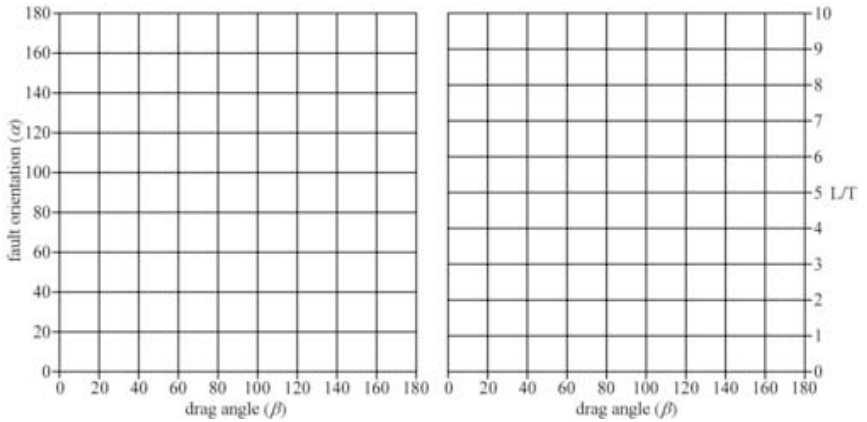

FigureA3
Click here to download high resolution image

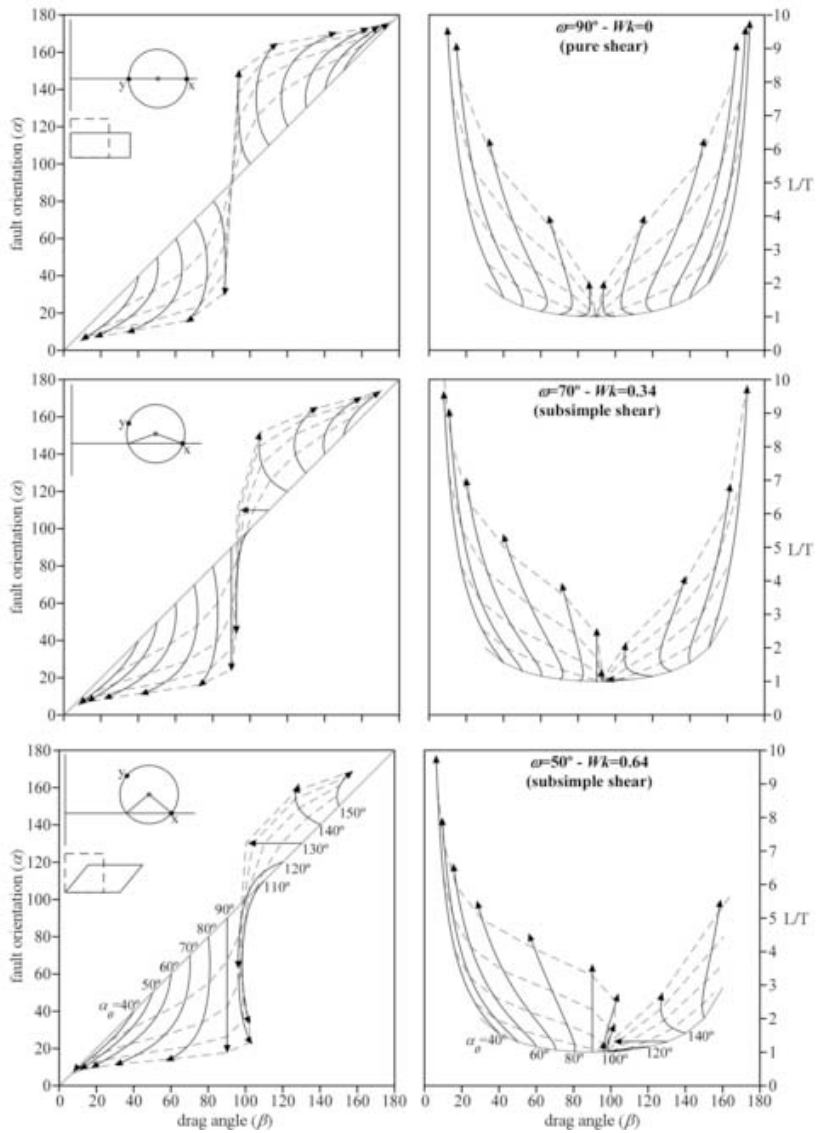

FigureA4
Click here to download high resolution image

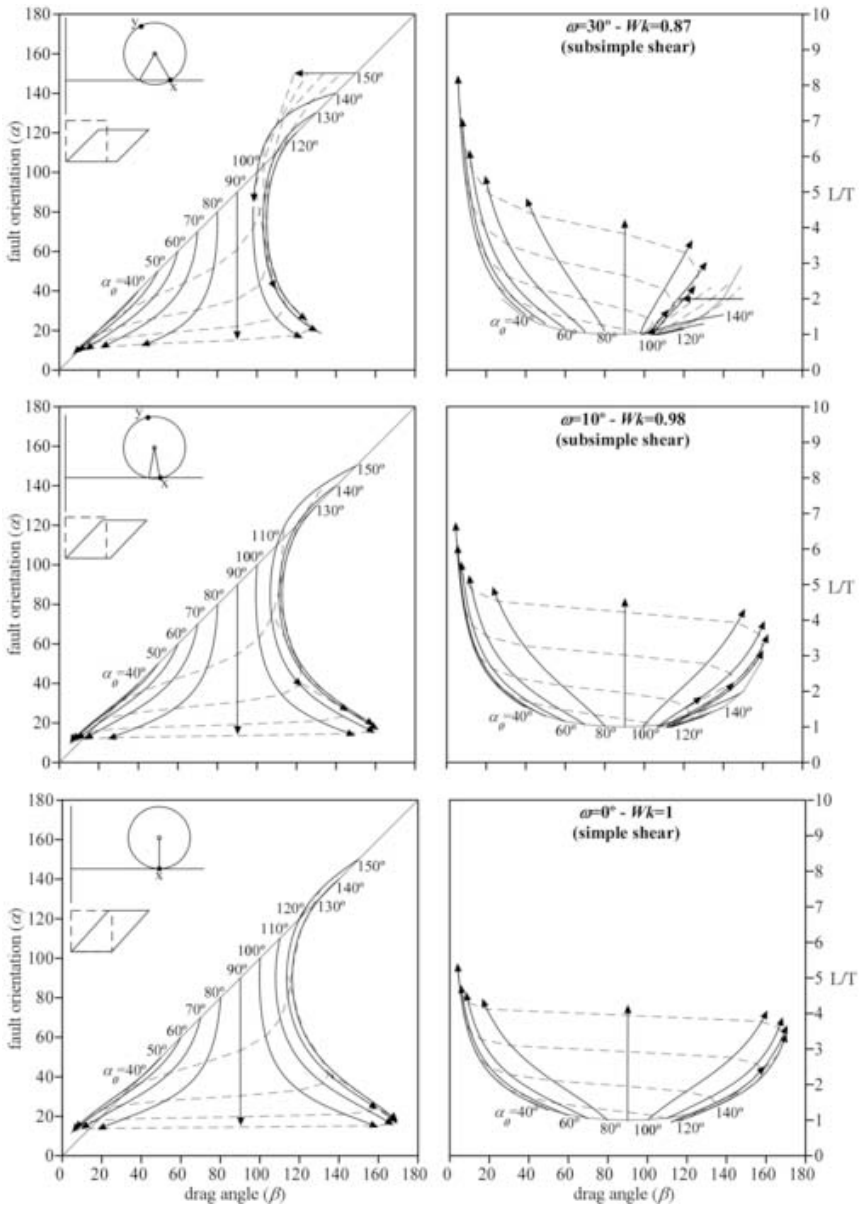

FigureA5
Click here to download high resolution image

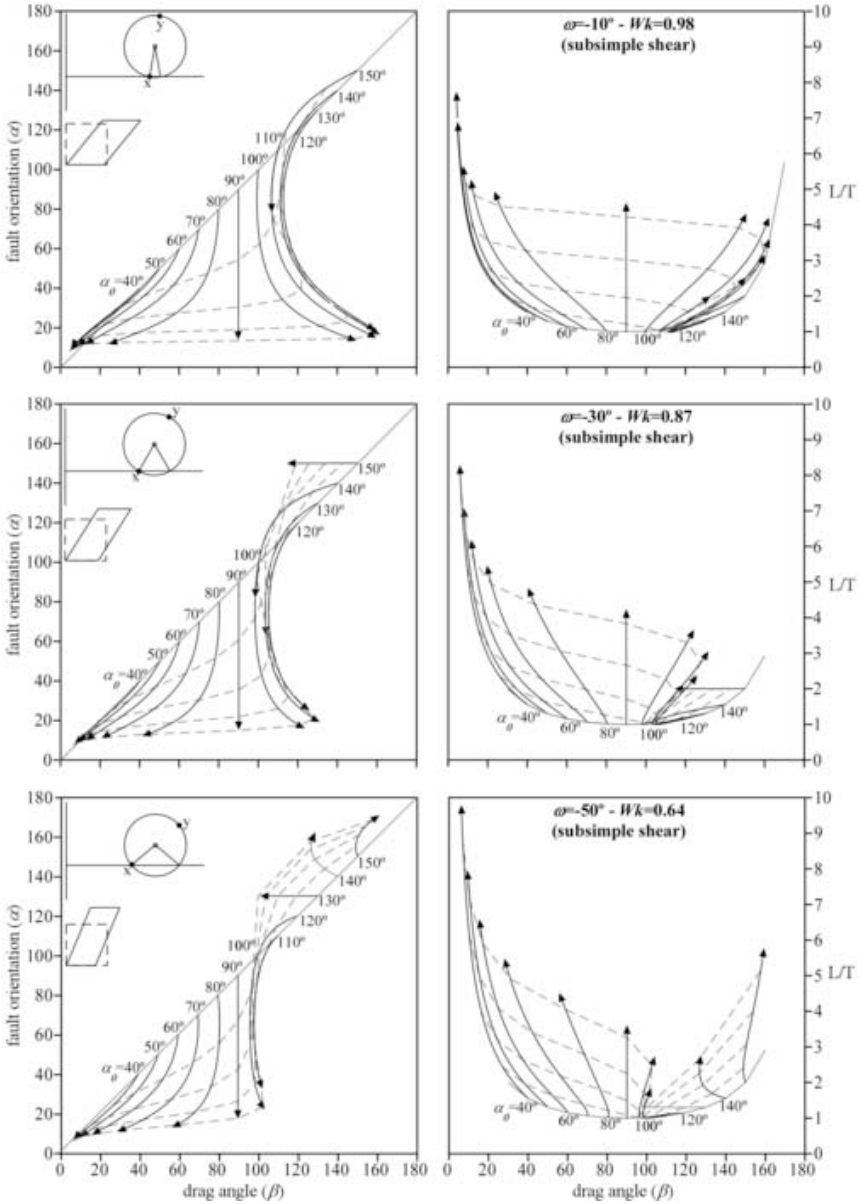

FigureA6
Click here to download high resolution image

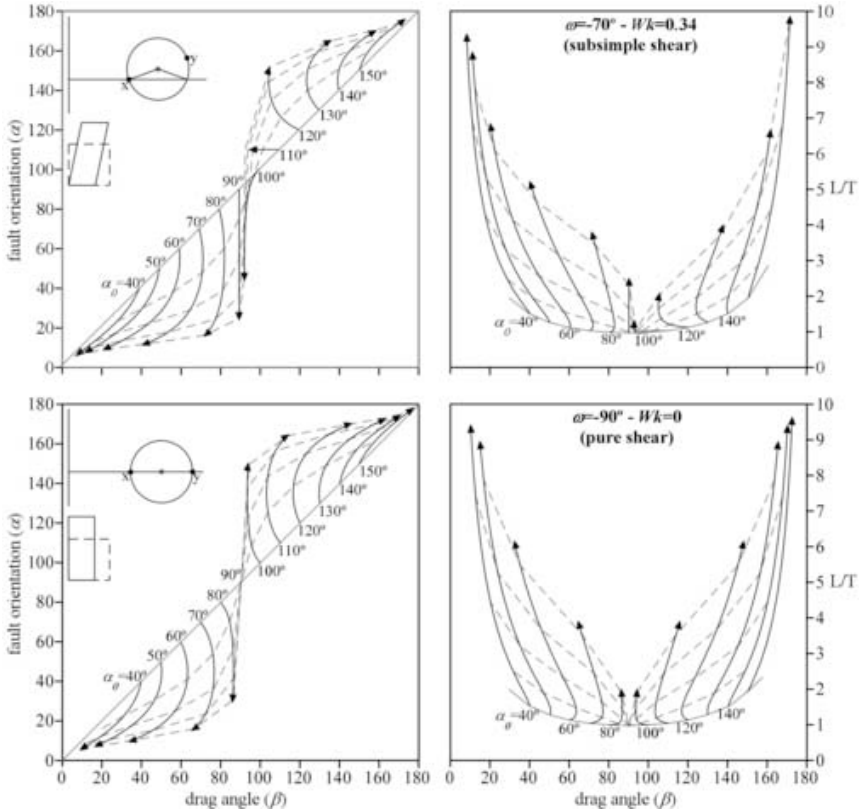

Table1

initial ω angle	initial Wk	calculated Wk	Wk error	initial α_0	calculated α_0	α_0 error
0º	1.00	0.92	**0.08**	45º	52.0º	**7.0º**
0º	1.00	1.00	**0.00**	75º	75.1º	**0.1º**
30º	0.87	0.79	**0.08**	45º	48.8º	**3.8º**
30º	0.87	0.86	**0.01**	75º	69.0º	**6.0º**
60º	0.50	0.48	**0.02**	45º	44.7º	**0.3º**
60º	0.50	0.58	**0.08**	75º	72.7º	**2.3º**
90º	0.00	0.01	**0.01**	45º	44.1º	**0.9º**
90º	0.00	0.10	**0.10**	75º	75.7º	**0.7º**

Table2

locality	data group	α_0	β_0	L/T
A	1	14	39	2.93
	2	36	67	1.93
B	3	53	77	1.56
C	4	21	28	2.81
	5	10	31	2.98
	6	28	61	1.89
	7	13	21	3.31
D	8	30	39	1.83
	9	26	53	1.50
	10	35	46	1.42
	11	33	50	1.75
	12	63	84	1.30
	13	26	60	1.65
	14	29	56	1.91
	15	19	49	1.95
	16	42	73	1.62
	17	54	66	1.28
	18	39	69	1.83
	19	64	81	0.94
	20	34	61	1.50
	21	36	52	1.71
	22	43	62	1.50
	23	21	54	2.13
E	24	27	41	1.71
	25	23	57	1.53
	26	22	26	2.42
	27	56	83	1.02
F	28	51	81	1.08
G	29	54	76	1.15